RSC Advances

PAPER

View Article Online
View Journal | View Issue

Cite this: *RSC Adv.*, 2015, **5**, 9667

Received 1st December 2014
Accepted 19th December 2014

DOI: 10.1039/c4ra15536j

www.rsc.org/advances

Doubling of electrochemical parameters *via* the pre-intercalation of Na^+ in layered MnO_2 nanoflakes compared to α-MnO_2 nanorods†

A. A. Radhiyah, M. Izan Izwan, V. Baiju, C. Kwok Feng, I. Jamil and R. Jose*

The pre-intercalation of Na^+ ions in layered birnessite-MnO_2 is shown to have a dramatic influence on its electrochemical properties. Electrochemical studies showed the doubling of the specific capacitance and energy density in the layered Na–MnO_2 nanoflakes compared to the MnO_2 nanorods.

1. Introduction

Materials with a layered structure exhibit unique or superior properties compared to their corresponding non-layered analogues. A few examples of the superior properties include: a higher superconducting transition temperature in layered cuprates, superior ion exchange in layered silicates, high photovoltaic conversion efficiency in layered perovskites, and high lithium storage capability in layered manganates. In particular, layered materials offer unique opportunities to significantly enhance their energy storage capability under the supercapacitive mode because their structure integrates different storage mechanisms, *viz.* electrochemical double layer capacitance (EDLC) and pseudocapacitance, in a single material.[1]

Transition metal oxides as pseudocapacitive electrodes are extensively investigated due to their potentially higher capacitance compared to conventional electrochemical double layer capacitors (EDLCs), which is mainly ascribed to their multiple oxidation states.[2] Due to the rarity of high performing pseudocapacitive materials, such as RuO_2, alternatives are actively sought. Many efforts are made on the use of MnO_2 as an electrode for Li-ion batteries[3] and electrochemical capacitors.[4] The use of MnO_2 as a supercapacitor electrode is highly desirable due to its merits, including low toxicity, environmental safety, cost effectiveness, and large capacitance.[2]

The MnO_6 octahedron is the basic building block of most Mn oxide crystals and their systems are assembled by sharing edges and/or corners in a large variety of different structural arrangements, most of which fall into one of two major groups: (1) chain, or tunnel, structures and (2) layered structures.[5] The layered Mn oxides consist of stacks of sheets, or layers, of edge-sharing MnO_6 octahedra. Owing to its relatively open structure, it is believed to provide more favorable pathways for the intercalation and deintercalation of protons or alkali metal cations as compared with monoclinic oxides.[6] One important strategy for improving electrode properties is the microstructural design of MnO_2 on the nanometer scale, such as nanoparticles,[7] nanotubes,[8] nanowires,[8] nanorods,[9–11] thin films,[6] and nanosheets.[2] Another main factor controlling the electrochemical performance of MnO_2 is the crystalline structure. Recently, α-MnO_2 has attracted considerable interest and its potential application as an electrode material for supercapacitors has been studied.[9,10,12] We have now observed a two-fold increase in the electrochemical performance of MnO_2 by the pre-intercalation of Na^+ ions in the layered structure of MnO_2.

The effort to pre-intercalate Na into layered structure MnO_2 has been discussed by other researchers.[13–16] However, pre-intercalation has been performed by different routes, such as electrodeposition,[13] solid-state reactions,[14,15,17] sol–gel,[16,18] hydrolysis,[19] molten salt-ion exchange,[20] hydrothermal,[21,22] and so on. The various morphologies and applications of Na–MnO_2 has been exhibited such as nanorods[19] (supercapacitor), and needle-like structures (sodium ion battery).[15] As studied by Sheng Liu *et al.*, $Na_2Mn_5O_{10}$ showed only 178 F g^{-1} at 0.1 A g^{-1} in a 1 M Na_2SO_4 electrolyte, which is lower than the results reported in this manuscript.[19] Meanwhile, Liqiang Mai *et al.* utilized the electrodeposition method to prepare the Na_xMnO_2 to be used in a supercapacitor.[13] Even though the electrode exhibited a high capacitance value, the adhesive and mass production problems are the shortcomings of electrodeposition method in preparing the electrode. However, our work used the facile hydrothermal route to produce Na–MnO_2 nanoflakes at a very low temperature.

2. Experimental details

2.1 Synthesis of α-MnO_2 nanorods and Na–birnessite MnO_2 nanoflakes

Manganese oxide materials with two different morphologies were synthesized through a facile hydrothermal route and

Nanostructured Renewable Energy Materials Laboratory, Faculty of Industrial Sciences & Technology, Universiti Malaysia Pahang, 26300 Kuantan, Pahang, Malaysia. E-mail: rjose@ump.edu.my

† Electronic supplementary information (ESI) available: FESEM images at high magnifications, CV of entire scan rate, galvanostatic charge–discharge curve, stability performance of three electrode system, fitted data of equivalent circuit, Ragone plot. See DOI: 10.1039/c4ra15536j

nanorods and nanoflakes were obtained. In a typical experimental procedure for the nanorod synthesis, 1.18 g of $KMnO_4$ and 2.112 g of Mn_2SO_4 were mixed using water as the medium. Then, the mixture was poured into a Teflon-lined stainless steel autoclave with a capacity of 200 ml and treated at 120 °C for 24 hours. The as-prepared sample was then dried in oven at 80 °C for 1 hour and is represented as MnO_2. However, for the nanoflakes synthetic route, 50 ml of a certain concentration of NaOH (1.25 M and 3.75 M) were added to the mixture as a sodium precursor before the hydrothermal treatment. After the autoclave cooled to room temperature, the black precipitates were collected by centrifugation and washed several times by deionized water to remove possible impurities or excess sodium ions. The as-prepared sample was then dried in an oven at 80 °C for 1 hour. The obtained samples were labeled Na–MnO_2(A) and Na–MnO_2(B), representing the different concentrations of 1.25 M and 3.75 M NaOH added, respectively.

2.2 Material characterization

The crystal structure of the prepared sample was studied by the X-ray diffraction (XRD) technique using a Rigaku Miniflex II X-ray diffractometer, employing Cu Kα radiation ($\lambda = 1.5406$ Å). The specific area measurement for the prepared sample was performed using the N_2 adsorption–desorption isotherm technique (Micromeritics, Model ASAP2020, USA). The morphology and microstructure of the materials were studied by scanning and transmission electron microscopic techniques. The shape and size of the samples were obtained using a field emission scanning electron microscope, JSM-7800F (JEOL, Japan) FESEM. N_2 adsorption and desorption experiments were carried out by employing an ASAP 2020 (Micromeritics, USA). The Brunauer–Emmett–Teller (BET) method was used to calculate the specific surface area, while the Barrett–Joyner–Halenda (BJH) analysis was done to investigate the porosity distribution.

2.3 Electrochemical measurements

For the electrochemical evaluation, a working electrode was prepared by mixing the active material with polyvinylidene fluoride (PVDF) (Sigma Aldrich, USA) and carbon black (Super P conductive, Alfa Aesar, UK) in a mass ratio of 85 : 5 : 10 and the mixture was stirred in *N*-methyl-2-pyrrolidinone (NMP) to achieve a homogeneous mixture. The resulting slurry was then pasted on a nickel foam substrate (current collector) and the electrode was dried at 60 °C for 24 hours. The dried electrode was then pressed using a pelletizer at 5 ton. A three-electrode system was used to evaluate the electrochemical performance by cyclic voltammetry (CV) using a potentiostat (Autolab PGSTAT 30, Eco Chemie B.V., The Netherlands) employing the NOVA 1.9 software in 1 M Na_2SO_4 aqueous electrolyte at room temperature. A platinum wire and a saturated Ag/AgCl electrode were used as the counter and the reference electrode, respectively. The supercapacitive performances of the samples were evaluated from the galvanostatic charge–discharge curves in the potential range of 0–1.0 V at different current densities (0.3, 0.5, 1, 2, 3, 5, 7 and 10 A g^{-1}) in 1 M Na_2SO_4 electrolyte. The kinetics at the electrode were studied using electrochemical impedance spectroscopy (EIS) using an Autolab Potentiostat.

An asymmetry two-electrode system was fabricated using commercial activated carbon (AC) as a negative electrode and Na–MnO_2(B) as a positive electrode. The best electrochemical performance in the three-electrode system was selected to setup a real two-electrode system. The composition of the carbon electrode is similar to the Na–MnO_2(B) electrode. However, the active mass of the activated carbon and Na–MnO_2(B) was determined by balancing the charge between the anode and cathode. To balance the mass ratio between the anode and cathode, the specific capacitance value of each material at a certain scan rate has to be determined using the equation below:

$$C_s = \frac{1}{mv(E_2 - E_1)} \int_{E_1}^{E_2} i(E)\delta E \quad (1)$$

Then, the mass ratio can be calculated by balancing the charge between the anode and cathode as shown below;

$$q_+ = q_- \quad (2)$$

$$C_s \times \Delta V \times m_+ = C_s \times \Delta V \times m_- \quad (3)$$

$$\frac{m_-}{m_+} = \frac{C_s(\mathrm{PC}) \times \Delta V_+}{C_s\ (\mathrm{EDLC}) \times \Delta V_-} \quad (4)$$

where q_+ and q_- is the charge stored at anode and cathode, ΔV is the potential window and C_s (EDLC) and C_s (PC) is the specific capacitance of each cathode and anode in the three-electrode configuration. The mass loading ratio of the asymmetric supercapacitor Na-MnO_2//AC for a 1 M Na_2SO_4 electrolyte system is 1.06, while in a 1 M KOH electrolyte system it is 1.66 (eqn (4)).

The specific capacitance of the electrode can be calculated through galvanostatic charge–discharge measurements using the following equation:

$$C_s = \frac{I\Delta t}{m\Delta V} \quad (5)$$

where C_s is the specific capacitance, I is the discharge current density in A, Δt is the discharge duration in s, m is the loaded mass of the active material in g, and ΔV is the potential range in V. The specific energy can be derived from the galvanostatic discharge curves using the following equation:

$$E = \frac{1}{2} C_s \Delta V^2 \quad (6)$$

where C_s is the specific capacitance (F) and ΔV is the potential window (V). The specific power of the electrode can also be calculated from the following equation:

$$P = \frac{E}{\Delta t} \quad (7)$$

3 Results and discussion

3.1 Synthesis and characterization of samples

The as-prepared MnO_2 had a rod-like morphology whereas the morphology changed to flake-like upon Na^+ intercalation. The

phase and crystal structure of the as-prepared samples were characterized by the powder X-ray diffraction (XRD) technique. All of the diffraction peaks of the as-prepared MnO_2 samples are indexed to a tetragonal α-MnO_2 structure (Fig. 1A), which is consistent with the JCPDS file no. 44-0141. The interlayer spacing of the α-MnO_2 is 6.77 nm at $2\theta = 13.06°$. The XRD patterns of Na–MnO_2(A) and Na–MnO_2(B) revealed the birnessite (δ-MnO_2) structure, which is consistent with the reference JCPDS (no: 13-0105). However, the lattice spacing for the layered structure of Na–MnO_2(A) is 6.75 nm, which corresponds to the diffraction peak at $2\theta = 13.10°$, and is less than Na–MnO_2(B) with 7.13 nm at $2\theta = 12.41°$. The more open lattice spacing of the layered structure could possibly be due to the increase of pre-intercalated Na^+ inside it. The FESEM image (Fig. 1B) shows that the nanostructured sample is comprised of nanorod structures with an average diameter of 30–60 nm. These nanorods were formed through a carefully controlled hydrothermal reaction by the redox reaction between $MnSO_4$ and $KMnO_4$.[23] The formation mechanism of the α-MnO_2 nanorods can be explained based on Wang and Li's theory; the MnO_x units in the solution goes through a condensation reaction to form δ-MnO_2 nanosheets, then curl with elevated temperatures and pressures to form one-dimensional nanostructures.[24] The lamellar structure of MnO_2 is in a metastable state, and δ-MnO_2 keeps its structure as enough K^+ was provided. If not enough cations are present, such as K^+ or NH_4^+, the layer structure will collapse into the 2 × 2 tunnel structure of α-MnO_2. Along with the phase transformation, the curling lamellar structures grow into nanorods. Due to the very long dwell time (~24 hours) of the hydrothermal treatment, the MnO_2 nanosheets changed to a nano-architecture with the formation of the nanorods. When the NaOH precursor is added to the synthetic route, the formation of nanorods is prevented. The modification of the synthetic route turned the morphology into nanoflake structures (Fig. 1C & D). This phenomenon can be explained by the replacement of K^+ by the pre-intercalated Na^+ in the layered structure of MnO_2. As the concentration of NaOH in the mixture increased, the formation of single nanosheets is obviously seen rather than agglomerate nanosheets. The high magnification FESEM images of the samples are shown in the ESI as Fig. S1.†

The surface area property of the samples was analysed using BET, which provides the precise specific surface area evaluation of materials by N_2 multilayer adsorption measured as a function of relative pressure using a fully automated analyser. The pore structure (*e.g.*, pore area, pore volume and pore diameter) was studied using the Barrett–Joyner–Halenda (BJH) analysis. The N_2 adsorption–desorption isotherm and BJH pore-size distribution by the BJH method are shown in Fig. 2A. According to the IUPAC classification, the isotherm of MnO_2 has the typical type II form with a small nitrogen hysteresis loop, Type H3. This indicates the existence of non-porous or macroporous structures, which is consistent with the dense nanorod structure. In contrast, the isotherm feature of other samples is classified as type IV, which indicates the presence of mesopores in the samples. The fraction of mesopores in Na–MnO_2(B) is large compared to Na–MnO_2(A) as indicated by the larger and clearer hysteresis loop of Na–MnO_2(B). The pore distribution curve showed that Na–MnO_2(B) has an abundance of mesopores with pore diameters between 2 and 40 nm (Fig. 2B).

The BET surface area, total pore volume and average pore diameter of the samples are summarized in Table 1. The high BET surface area obtained and the wide distribution of the mesopore structures of Na–MnO_2(B) can allow the efficient transport of electrons and ions, thereby leading to the high electrochemical capacity of the electrode material.

3.2 Electrochemical properties

The electrodes for the electrochemical studies were prepared by pasting the active materials on Ni foam substrates. The electrochemical properties of the electrodes were tested in the three-electrode configuration using 1 M Na_2SO_4 as the electrolyte, Ag/AgCl as the reference electrode and Pt wire as the counter electrode. Fig. 3A–C shows the comparison of the cyclic voltammograms (CVs) of each studied material at low scan rates (5, 10 and 25 mV s^{-1}) within a 0–0.9 V working potential. The CV measurements were also conducted at different scan rates ranging from 5 to 100 mV s^{-1} (Fig. S2, ESI†). The current response of the CV for Na–MnO_2(A) and Na–MnO_2(B) is almost double compared to that of MnO_2. For MnO_2, the shape of CV shows the approximate rectangular mirror image characteristic of capacitive behaviour, which exhibits a pseudo-constant rate

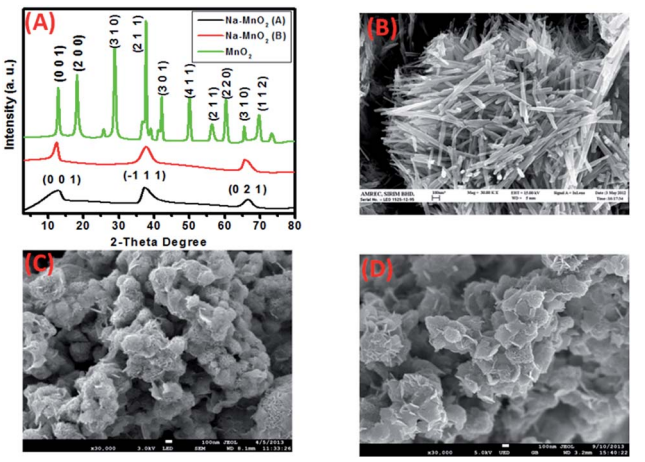

Fig. 1 (A) XRD profiles of samples, (B)–(D) FESEM image of MnO_2, Na–MnO_2(A), and Na–MnO_2(B), respectively.

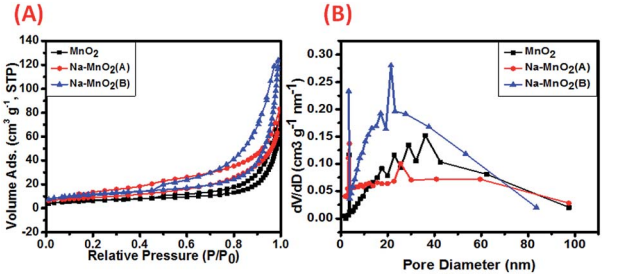

Fig. 2 (A) N_2 adsorption–desorption isotherm and (B) pore diameter distribution curve of samples.

Table 1 Summary of BET surface area, total pore volume and average pore diameter of the samples

Sample	Surface area ($m^2\ g^{-1}$)	Pore volume ($cm^3\ g^{-1}$)	Pore diameter (nm)
MnO_2	23.1	0.12	18
Na–MnO_2(A)	31.3	0.13	8.8
Na–MnO_2(B)	41.0	0.19	12.6

over the entire CV test. The rectangular shape without redox peaks in the CV curve is due to the difficult and long distance Na^+ diffusion in the MnO_2 interlayers. Fig. 2D shows the obtained profiles of the galvanostatic charge–discharge measurements at 0.3 A g^{-1} for all of the samples. The good symmetry and near-linear slope in both the charge and discharge branches again support the idea that the MnO_2 electrode is electrochemically reversible and possesses excellent capacitive characteristics. Different observations were obtained for Na–MnO_2(A) and Na–MnO_2(B) at low scan rates. A deviation from the symmetrical shape was observed at 5 to 25 mV s^{-1}. The observed redox peaks in the Na–MnO_2(A) and Na–MnO_2(B) electrodes are attributed to the pre-intercalation effect. The pre-intercalation of Na^+ expedites the succeeding electrochemical ion diffusion, intercalation/deintercalation and transport process, resulting in the redox process of Mn between Mn^{4+} and Mn^{3+}. The as-observed redox peaks in the CV curves at 0.4–0.7 V (*vs.* Hg/HgO) are exactly identical with the theoretical transformation potential between Mn^{4+} and Mn^{3+} due to the reversible intercalation/deintercalation of Na^+ ions in Na–MnO_2(B). In addition, the larger specific surface area of Na–MnO_2(B) implies more Faradaic active sites and thereby a higher pseudocapacitance.[25]

Galvanostatic charge–discharge measurements were performed at current densities between 0.3 and 10 A g^{-1} to evaluate the ability of the material nanostructures as a pseudocapacitor electrode (Fig. S3, ESI†). The variation of C_s at different current densities for all of the samples is shown in the ESI as Fig. S4.† From the values obtained, it can be concluded that the electrochemical performance of Na–MnO_2(B) is almost doubled as compared to α-MnO_2. Significantly, the pre-intercalation of Na^+ into the open layered structure of MnO_2 facilitates the diffusion and transport process of anions to the inner active sites, indicating a pseudocapacitance behaviour which results from the electrochemical adsorption–desorption or redox reactions at the electrode–electrolyte interface. This hybrid charge storage mechanism in layered materials was recently shown to be suitable in high energy density supercapacitor applications.[1] The more open lattice spacing of the layered structure contributes to the more specific capacitance value as shown by the difference in values between Na–MnO_2(A) and Na–MnO_2(B). The Ragone-plots of these materials as supercapacitor electrodes at different current densities are shown in the ESI as Fig. S4.† In the case of MnO_2, Na–MnO_2(A) and Na–MnO_2(B) exhibited almost similar power densities of 150, 150 and 167 W kg^{-1}, but with different energy densities of 14, 24 and 27 W h kg^{-1}, respectively. The galvanostatic charge–discharge curves of these samples are also shown in the ESI as Fig. S5.†

In order to further investigate the electrochemical behavior of the materials, EIS measurements were performed at an open circuit potential as shown in Fig. 2E. The well-fitted equivalent circuit plot of all three samples and the equivalent circuit employed for fitting are shown as Fig. S6 in the ESI.† A simplified equivalent circuit consists of R_s, R_{ct}, CPE1, W and CPE2. The R_s is the solution resistance, CPE1 and CPE2 are the constant phase element for double layer capacitance and pseudocapacitance, R_{ct} is the charge transfer resistance and W is the Warburg diffusion resistance. Fig. 3E, including the inset figure, shows that all of the samples are similar in shape, demonstrating a partial semicircle at the high frequency region and a near-vertical line in the low frequency region. The semicircle portion corresponds to the combination of electrolyte resistance (R_s) and charge transfer resistance (R_{ct}) and the slope of the line indicates the Warburg impedance (Z_w), which represents the diffusive behaviors of the electrolyte pores and ions in the active materials. The equivalent series resistance (ESR) is determined from the intercept value at the x-axis of the semicircle. From the inset of Fig. 3E, the lowest ESR value is obtained for sample Na–MnO_2(B) (~1.01 Ω) compared to that of Na–MnO_2(A) (~2.64 Ω) and MnO_2 (~2.60 Ω). A small ESR is expected due to the well-formed nanosheet structure, which facilitates the efficient access of electrolyte ions to the Na–MnO_2(B) surface and shortening the ion diffusion, subsequently enhancing the electrochemical properties of the devices. The lowest R_{ct} value, which is determined by the diameter of the semicircle is obtained for MnO_2 (~0.5 Ω), compared to that of Na–MnO_2(A) (~2.5 Ω) and Na–MnO_2(B) (~1.5 Ω). Fig. 3F shows the evolution of the imaginary portion of the capacitance *versus* frequency. From the plot, a peak is observed at certain values with frequency. The relaxation time, which can be determined from this peak is defined as the boundary between the regions of capacitive and resistive behaviors for the supercapacitor. From the calculation, the τ of the samples are 0.01 s, 0.004 s, and 0.003 s for sample MnO_2, Na–MnO_2(A) and Na–MnO_2(B), respectively. A lower τ contributes to higher power delivery.

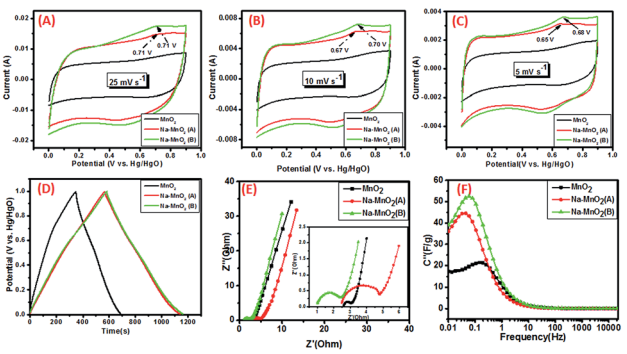

Fig. 3 (A)–(C) CV profiles of the samples at 25, 10 and 5 mV s^{-1}, (D) charge–discharge profile of samples at 0.3 A g^{-1}, (E) Nyquist plot of the samples (inset: expanded high-frequency region of the plot), (F) evolution of the imaginary part of the capacitance *versus* the frequency.

The Na^+ ion diffusion coefficient (D_{Na^+}) in each sample was calculated using the Randles–Sevcik equation to prove the facilitated Na^+ diffusion by pre-intercalation as stated below:[26]

$$i_p = 2.69 \times 10^5 \times n^{\frac{3}{2}} \times A \times D^{\frac{1}{2}} \times C_0 \times v^{\frac{1}{2}} \quad (8)$$

where i_p is the peak current, n is the number of electrons, F is the Faraday constant, T is the temperature in Kelvin, R is the gas constant, A is the surface area of the working electrode, D is the diffusion coefficient of the electroactive species, C is the bulk concentration of the electroactive species and v is the scan rate of the voltammograms. The Na^+ diffusion coefficients in MnO_2, Na–MnO_2(A) and Na–MnO_2(B) are calculated from the slope of the plot of i_p *versus* $\sqrt{v}$ (Fig. 4). It can be seen from the figure that the slope of i_p *versus* $\sqrt{v}$ are in the order of Na–MnO_2(B) > Na–MnO_2(A) > MnO_2, indicating a high proton diffusion coefficient trend in the order of Na–MnO_2(B) > Na–MnO_2(A) > MnO_2. A high proton diffusion coefficient enhances the ion transportation (Na^+), thereby accelerating the electrode redox reaction. The D_{Na^+} was calculated to be 5.0×10^{-14} cm^2 s^{-1}, 1.5×10^{-13} cm^2 s^{-1} (A), 2.3×10^{-13} cm^2 s^{-1} for MnO_2, Na–MnO_2(A) and Na–MnO_2(B), respectively. Na–MnO_2(B) has the highest proton diffusion coefficient which indicates fast Na^+ transportation into the matrix of the electrode material because of high Na^+ pre-intercalation in the layered structure. It is proven that the higher capacitance originated from the diffusion of ions inside the layered structure of the Na–MnO_2(B) nanoflakes, which then triggered the redox reaction and in agreement with the CV profiles for these samples. The EIS curve also shows that the reaction is diffusion-controlled because the straight line at the low frequency deviated towards 45°. However, a more capacitive nature was observed for the MnO_2 sample as shown by the symmetrical shape of the CV profiles and nearly straight line at the low frequency region of the EIS curve. However, due to the low surface area of MnO_2, its capacitance value is not higher than the two other Na–MnO_2 samples as they have capacitive and diffusive behaviours in the charge storage mechanism.

To further explore the electrochemical performance of Na–MnO_2(B) in a real system, an asymmetric two-electrode configuration was assembled using Na–MnO_2(B) as the positive electrode (potential window of 0–0.9 V in 1 M Na_2SO_4 and −0.45–+0.45 V in 1 M KOH) and activated carbon as the negative electrode (potential window of −0.9 to 0 V). The CV curve for Na–MnO_2(B) and commercial activated carbon (AC) in a three-electrode system of 1 M Na_2SO_4 and 1 M KOH electrolyte is shown in the ESI as Fig. S7.† To construct an asymmetric supercapacitor, the loading mass ratio of active materials was determined by balancing the charge between the cathode and the anode electrode. Balancing the mass of these two materials with pseudo-capacitive properties results in a practical cell voltage of 2.0 V in 1 M Na_2SO_4, and up to 1.6 V in 1 M KOH with an energy density close to the values obtained with EDLCs working in organic electrolytes, while avoiding their disadvantages. To balance the charge, the specific capacitance of each electrode in the three-electrode configuration must be determined from cyclic voltammetry measurements. Both asymmetry cells exhibited an ideal capacitive behaviour with perfectly rectangular CV curves without any redox peaks (Fig. 5A and B). The cyclic voltammetry measurements demonstrated the good charge–discharge properties and rate capability of the asymmetric supercapacitor as shown by the galvanostatic charge–discharge curve (Fig. 5C). The capacitance of the asymmetric supercapacitor was calculated to be 120 F g^{-1} (1 M Na_2SO_4) and 176 F g^{-1} (1 M KOH) based on the total weight of the electrodes at the current density of 0.3 A g^{-1} (Fig. 5D). The supercapacitor delivered an energy density of 24 and 16 W h kg^{-1} in 1 M Na_2SO_4 and 1 M KOH, respectively as shown in the Ragone plot (Fig. S7, ESI†). These values are also comparable to those of transition metal oxide-based asymmetric cells with a mild aqueous electrolyte, such as MnO_2//graphene (25.2 W h kg^{-1}),[27] MnO_2 + carbon//carbon (30 W h kg^{-1}),[28] MnO_2//graphene hydrogel (23.2 W h kg^{-1}),[29] MnO_2 + AMC//graphene (18.0 W h kg^{-1}),[30] $Co(OH)_2$//AC (13.6 W h kg^{-1}),[31] AC//$NaMnO_2$ (19.5 W h kg^{-1})[32] and so on. The asymmetric AC//Na–MnO_2(B) supercapacitor shows a reasonable cycling behavior (Fig. 6). A capacitance loss (~10%) is observed at the initial cycles then become stable for the remaining cycles up to 10 000 cycles at the current density of 0.3 A g^{-1} between 0 and 2.0 V.

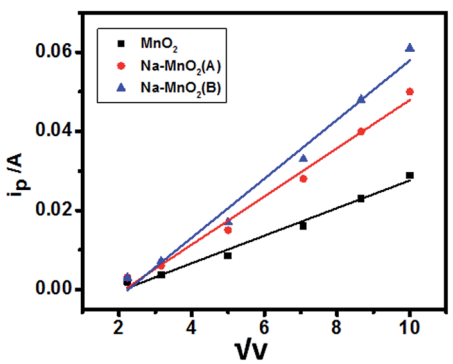

Fig. 4 Peak current *versus* the square root of the scan rate.

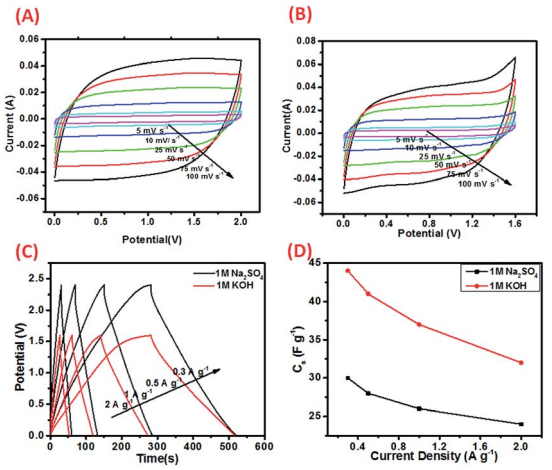

Fig. 5 (A and B) CV profiles of Na–MnO_2(B)//AC asymmetry cell, (C) galvanostatic charge–discharge curves and (D) C_s *versus* current density in 1 M Na_2SO_4 and 1 M KOH, respectively.

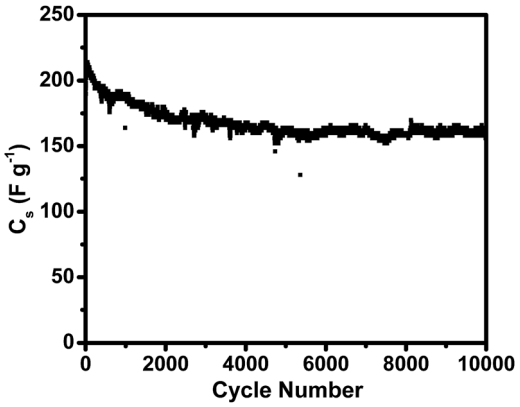

Fig. 6 Cycling performance of the asymmetric assembly of Na-MnO_2(B)//AC in 1 M Na_2SO_4 at current density 0.3 A g^{-1}.

The contribution of pre-intercalated Na^+ in the layered structure to the electrochemical performance can be clearly explained through charge storage mechanism in Fig. 3. α-MnO_2 is constructed of a 2 × 2 tunnel with a radius of 3.44 Å (Fig. 7A). However, the radius of solvated Na^+ (3.58 Å) is larger than the radius of the tunnel. Therefore, the cation has difficulty to reside at the center of the tunnel during the first charging process. The radius of solvated Na^+ is smaller than the interlayer spacing of the layered structure, thus it is possible that the intercalation/deintercalation process occurred.[33]

For layered δ-MnO_2 without any Na^+ pre-intercalation (Fig. 7B), even though the solvated Na^+ radius is smaller than the layered spacing, the cation will only reside in the thin layer of MnO_2 during the first charging and then diffuse out during discharging. Therefore, the layered δ-MnO_2 only exhibits a pseudo-constant rate over the entire CV test. It is due to the difficult and long distance Na^+ diffusion in the MnO_2 interlayers, in response to the rectangular shape without redox peaks in the CV curve even at low scan rates. But, the case is different for the pre-intercalated Na in δ-MnO_2 (Fig. 7C), at the first charge, the existing Na^+ ions during synthesis may deintercalate from the interlayer and the intercalation of H_2O might happen concomitantly. Following the discharge process, the cations in the electrolytes are supposed to intercalate into the interlayer and stabilize the layered structure. Because of the wider interlayer spacing (d), the diffusion of Na^+ cations into the Faradaic

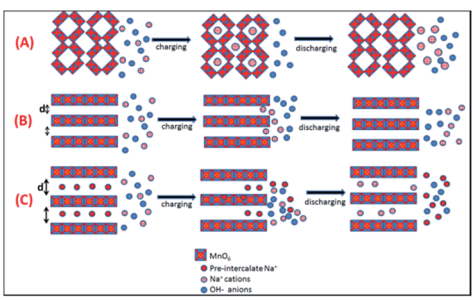

Fig. 7 Schematic process of charging–discharging for (A) tunnel α-MnO_2, (B) layered δ-MnO_2 and (C) pre-intercalation of Na^+ in δ-MnO_2.

active sites improved, thereby producing a higher pseudocapacitance. This proved that Na–MnO_2 shows the largest capacitance due to the fact that the reversible intercalation/deintercalation of Na^+ in the solid phase produces an additional capacitance besides the capacitance based on the absorption–desorption reaction.[34]

4. Conclusions

In summary, we used a facile free-template hydrothermal method to prepare pre-intercalated Na in δ-MnO_2 with a nanoflake morphology, which presents a better electrochemical behavior than the rod-like sodium-free MnO_2 in the three-electrode configuration using 1 M Na_2SO_4 aqueous solution as the electrolyte. The capacitance of the nanoflake Na–MnO_2(A) (~173 F g^{-1}) and Na–MnO_2(B) (~200 F g^{-1}) is much higher than that of the rod-like MnO_2 (~102 F g^{-1}). The two Na–MnO_2 samples deliver an energy density 24 W h kg^{-1} and 27 W h kg^{-1} at a power density of 150 W kg^{-1} and 167 W kg^{-1}, which is higher than that of the rod-like MnO_2, 14 W h kg^{-1} at a power density of 150 W kg^{-1}. Additionally, the application of Na–MnO_2(B) in the two-electrode configuration delivered an energy density of 24 and 16 W h kg^{-1} in 1 M Na_2SO_4 and 1 M KOH, respectively.

Acknowledgements

This project is supported by the Malaysian Technological University Network (MTUN).

Notes and references

1 R. A. Aziz, I. I. Misnon, K. F. Chong, M. M. Yusoff and R. Jose, *Electrochim. Acta*, 2013, **113**, 141–148.
2 M. Yano, S. Suzuki, M. Miyayama and M. Ohgaki, *Solid State Ionics*, 2013, **233**, 32–37.
3 X. Liu, C. Chen, Y. Zhao and B. Jia, *J. Nanomater.*, 2013, DOI: 10.1155/2013/736375.
4 G. Wang, G. Shao, J. Du, Y. Zhang and Z. Ma, *Mater. Chem. Phys.*, 2013, **138**, 108–113.
5 H. Welfare, *Proc. Natl. Acad. Sci. U. S. A.*, 1999, **96**, 3447–3454.
6 D. P. Dubal, D. S. Dhawale, R. R. Salunkhe, S. M. Pawar and C. D. Lokhande, *Appl. Surf. Sci.*, 2010, **256**, 4411–4416.
7 R. Jiang, T. Huang, J. Liu, J. Zhuang and A. Yu, *Electrochim. Acta*, 2009, **54**, 3047–3052.
8 H. Xia, J. Feng, H. Wang, M. O. Lai and L. Lu, *J. Power Sources*, 2010, **195**, 4410–4413.
9 Y. Li, H. Xie, J. Wang and L. Chen, *Mater. Lett.*, 2011, **65**, 403–405.
10 T. Yousefi, A. Nozad, M. Hossein and M. Aghazadeh, *J. Solid State Chem.*, 2012, **190**, 202–207.
11 L. Yuan, X. Lu, X. Xiao, T. Zhai, J. Dai, F. Zhang, B. Hu and X. Wang, *ACS Nano*, 2012, **6**(1), 656–661.
12 H. Wang, D. Qian, Z. Lu, Y. Li, R. Cheng and W. Zhang, *J. Cryst. Growth*, 2007, DOI: 10.1016/j.jcrysgro.2007.01.034.
13 L. Mai, H. Li, Y. Zhao, L. Xu, X. Xu, Y. Luo, Z. Zhang, W. Ke, C. Niu and Q. Zhang, *Sci. Rep.*, 2013, **3**, 1–8.

14 V. V. De, E. A. Pomerantseva, T. L. Kulova, A. V. Grigorieva, A. M. Skundin, E. A. Goodilin and Y. D. Tretyakova, *Mendeleev Commun.*, 2009, **19**, 187–189.
15 J. F. Whitacre, A. Tevar and S. Sharma, *Electrochem. Commun.*, 2010, **12**, 463–466.
16 A. Caballero, L. Hernán, J. Morales, L. Sánchez, J. Santos Peña and M. A. G. Aranda, *J. Mater. Chem.*, 2002, **12**, 1142–1147.
17 X. Ma, H. Chen and G. Ceder, *J. Electrochem. Soc.*, 2011, **158**, A1307.
18 M. Hibino, H. Kawaoka, H. Zhou and I. Honma, *Electrochim. Acta*, 2004, **49**, 5209–5216.
19 S. Liu, C. Fan, Y. Zhang, C. Li and X. You, *J. Power Sources*, 2011, **196**, 10502–10506.
20 F. Hu and M. M. Doeff, *J. Power Sources*, 2004, **129**, 296–302.
21 X.-M. Liu, Z.-D. Huang, S.-W. Oh, P.-C. Ma, J. Ma, B.-H. Li and J.-K. Kim, *J. Nanosci. Nanotechnol.*, 2010, **10**, 7378–7381.
22 X. Zhang, W. Yang, X. Chen and Y. Ma, *J. Nanosci. Nanotechnol.*, 2009, **9**, 5860–5864.
23 N. Tang, X. Tian, C. Yang, Z. Pi and Q. Han, *J. Phys. Chem. Solids*, 2010, **71**, 258–262.
24 W. X. Y. Li, *Chem.–Eur. J.*, 2003, **9**, 300–306.
25 G. Wang, L. Zhang and J. Zhang, *Chem. Soc. Rev.*, 2012, **41**, 797–828.
26 B. Shruthi, V. Bheema Raju and B. J. Madhu, *Spectrochim. Acta, Part A*, 2015, **135**, 683–689.
27 J. Cao, Y. Wang, Y. Zhou, J.-H. Ouyang, D. Jia and L. Guo, *J. Electroanal. Chem.*, 2013, **689**, 201–206.
28 J.-G. Wang, Y. Yang, Z.-H. Huang and F. Kang, *Carbon*, 2013, **61**, 190–199.
29 H. Gao, F. Xiao, C. B. Ching and H. Duan, *ACS Appl. Mater. Interfaces*, 2012, **4**, 2801–2810.
30 S. Zhu, W. Cen, L. Hao, J. Ma, L. Yu, H. Zheng and Y. Zhang, *Mater. Lett.*, 2014, **135**, 11–14.
31 Y. Tang, Y. Liu, S. Yu, S. Mu, S. Xiao, Y. Zhao and F. Gao, *J. Power Sources*, 2014, **256**, 160–169.
32 Q. T. Qu, Y. Shi, S. Tian, Y. H. Chen, Y. P. Wu and R. Holze, *J. Power Sources*, 2009, **194**, 1222–1225.
33 I. I. Misnon, R. A. Aziz, N. K. M. Zain, B. Vidhyadharan, S. G. Krishnan and R. Jose, *Mater. Res. Bull.*, 2014, **57**, 221–230.
34 O. Ghodbane, J.-L. Pascal and F. Favier, *ACS Appl. Mater. Interfaces*, 2009, **1**, 1130–1139.